INTERNATIONAL JOURNAL FOR NUMERICAL METHODS IN FLUIDS
Int. J. Numer. Meth. Fluids 2007; **53**:1819–1845
Published online 25 October 2006 in Wiley InterScience (www.interscience.wiley.com). DOI: 10.1002/fld.1384

Numerical simulation of natural and mixed convection flows by Galerkin-characteristic method

Mofdi El-Amrani[1,*,†] and Mohammed Seaïd[2]

[1]*Departmento Matemáticas, Universidad Rey Juan Carlos, c/Tulipán s/n, Mostoles-Madrid 28933, Spain*
[2]*Universität Kaiserslautern, Fachbereich Mathematik, Kaiserslautern 67663, Germany*

SUMMARY

A numerical investigation is performed to study the solution of natural and mixed convection flows by Galerkin-characteristic method. The method is based on combining the modified method of characteristics with a Galerkin finite element discretization in primitive variables. It can be interpreted as a fractional step technique where convective part and Stokes/Boussinesq part are treated separately. The main feature of the proposed method is that, due to the Lagrangian treatment of convection, the Courant–Friedrichs–Lewy (CFL) restriction is relaxed and the time truncation errors are reduced in the Stokes/Boussinesq part. Numerical simulations are carried out for a natural convection in squared cavity and for a mixed convection flow past a circular cylinder. The computed results are compared with those obtained using other Eulerian-based Galerkin finite element solvers, which are used for solving many convective flow models. The Galerkin-characteristic method has been found to be feasible and satisfactory. Copyright © 2006 John Wiley & Sons, Ltd.

Received 20 February 2006; Revised 11 July 2006; Accepted 15 July 2006

KEY WORDS: natural convection; mixed convection; modified method of characteristics; Galerkin finite element method

1. INTRODUCTION

Natural and mixed convection flows are encountered in various engineering systems, such as solar thermal receivers, electronic cooling devices, microwave ovens, crystal growth, fire in buildings, etc. The governing equations of fluid flow and heat transfer, in most of these problems, are the incompressible Navier–Stokes/Boussinesq equations. These equations are the subject of very intensive research activities since they include a wide variety of difficulties which typically arise in

*Correspondence to: Mofdi El-Amrani, Departmento Matemáticas, Universidad Rey Juan Carlos, c/Tulipán s/n, Mostoles-Madrid 28933, Spain.
†E-mail: mofdi.elamrani@urjc.es

Contract/grant sponsor: Universidad Rey Juan Carlos; contract/grant number: GDV-04-3

the computational fluid dynamics. Numerical treatment of these equations often present difficulties due to their non-linear form, incompressibility condition, presence of the convective term, coupling between the energy equation and the equations governing the fluid motion. In many thermal incompressible Navier–Stokes problems, the convective term is distinctly more important than the diffusive term; particularly when the Rayleigh or Reynolds numbers reach high values, this convective term is a source of computational difficulties and non-physical oscillations.

There exists a variety of computational methods available in the literature. For instance, applied to convection-dominated flows, Eulerian methods incorporate some upstream weighting in their formulations to stabilize the numerical procedure. The most popular Eulerian methods, in finite element framework, are the streamline upwind Petrov–Galerkin, Galerkin/least-squares and Taylor–Galerkin methods. All these Eulerian methods are easy to formulate and implement. However, time truncation errors dominate their solutions and are subjected to Courant–Friedrichs–Lewy (CFL) stability conditions, which put a restriction on the size of time steps taken in numerical simulations. Galerkin-characteristic methods (also known by semi-Lagrangian methods in meteorological community) on the other hand, make use of the transport nature of the governing equations. The idea in these methods is to rewrite the governing equations in term of Lagrangian co-ordinates as defined by the particle trajectories (or characteristics) associated with the problem. Then, the Lagrangian total derivative is approximated, thanks to a divided difference operator. The Lagrangian treatment in these methods greatly reduces the time truncation errors in the Eulerian methods [1]. In addition, these methods are known to be unconditionally stable, independent of the diffusion coefficient, and optimally accurate at least when the inner products in the Galerkin procedure are calculated exactly [2].

In Galerkin-characteristic methods, the time derivative and the advection term are combined as a directional derivative along the characteristics, leading to a characteristic time-stepping procedure. Consequently, the Galerkin-characteristic methods symmetrize and stabilize the governing equations, allow for large time steps in a simulation without loss of accuracy, and eliminate the excessive numerical dispersion and grid orientation effects present in many upwind methods [3, 4]. A Galerkin-characteristic algorithm has been successfully applied to isothermal Navier–Stokes equations in [5]. The current work presents an extension of the method to thermal viscous incompressible flows. To the best of our knowledge, there are no detailed computational studies on natural and mixed convection flows using Galerkin-characteristic methods. The results of such studies are useful for providing comparative data and developing robust solvers for heat transfer and fluid flow computations.

A class of Galerkin-characteristic methods has been investigated in References [2, 3, 6, 7], among others. In [2], a first-order characteristics method combined with finite element method has been analysed for the isothermal incompressible Navier–Stokes equations. It has been shown that the method is unconditionally stable provided the characteristics are transported by divergence-free field that is deduced from the flow velocity. The case where the characteristics are transported by discrete velocity field which is not divergence-free has been studied in [6]. Analysis of modified method of characteristics using finite difference discretization has been treated in [3] for convection–diffusion equations. In the finite difference framework, modified method of characteristics has also been experimented in [8–10]. Combining modified method of characteristics with spectral method has been investigated in [7] for hyperbolic problems. In all these references the convergence and stability of the method are proven under the assumption that all the inner products are calculated exactly. Furthermore, the evaluation of the fluid particles at the departure points in [2, 3, 6] is performed using an L^2-projection on the finite element space. In many applications, the evaluation

DOI: 10.1002/fld

of integrals in the L^2-projection is the most difficult part of these approaches. The current method differs from the approaches in [2, 3, 6] in the fact that (i) solutions at the characteristic feet are approximated by interpolation from finite element basis functions and (ii) the time integration is based on a second-order scheme instead of the first-order backward method used in [2, 3, 6].

The main goal of this work is to combine the modified method of characteristics and finite element method for solving natural and mixed convection problems. This numerical technique associates the geometrical flexibility of the finite elements with the stability offered by the modified method of characteristics. In addition, an advantage of combining finite element method with the modified method of characteristics is that interpolation procedures at the characteristic feet can be performed using the finite element basis functions. Obviously, this will reduce the computational cost and requires less implementation work than using the L^2-projection on the corresponding spaces. Furthermore, the method is suitable for complex geometries, independent of the sizes and arrangement of the mesh elements, and can easily combine different polynomial orders of elements.

The results using the Galerkin-characteristic methods are presented for two test problems. The first example is the natural convection in a squared cavity at Rayleigh numbers up to 10^8. The second example is the mixed convection flow past a circular cylinder at several Reynolds numbers. We present elaborated comparisons, in terms of accuracy and efficiency, between the Galerkin-characteristic methods and their Eulerian counterparts traditionally used in the literature for incompressible Navier–Stokes equations.

The present paper is organized as follows. We first give a brief description of the model employed. In Section 3, we then formulate the Galerkin-characteristic finite element method. Numerical results are presented in Section 4. Conclusions are drawn in Section 5. For sake of completeness, the Eulerian-based Galerkin finite element methods used for comparison are described in the Appendix.

2. THE GOVERNING EQUATIONS

In the present work, we consider convection flows consisting of a Boussinesq approximated viscous Newtonian fluid flowing in a bounded domain Ω with boundary Γ subject to a thermal variation $(T'_{\mathrm{H}} - T'_{\mathrm{C}})$, where T'_{H} and T'_{C} are temperatures of the hot and cold boundary regions on Γ. Here and in what follows primed variables refer to dimensional quantities. The Newtonian assumption guarantees a linear dependence between the shear stress and the velocity gradient, while the Boussinesq approximation ensures that the density differences are confined to the buoyancy force without violating the incompressibility condition. For more details on physical aspects of thermal flows we refer the reader to [11, 12] and further references can be found therein. In the present work, we consider the unsteady Navier–Stokes/Boussinesq equations to be solved for the velocity field $\mathbf{u}'$, the pressure p' and the temperature T'. The governing equations are:
continuity equation:

$$\nabla \cdot \mathbf{u}' = 0 \tag{1}$$

momentum equation:

$$\rho_\infty \left(\frac{\partial \mathbf{u}'}{\partial t'} + \mathbf{u}' \cdot \nabla \mathbf{u}' \right) + \nabla p' = \mu \Delta \mathbf{u}' + \rho_\infty (1 - \beta'(T' - T'_\infty))\mathbf{g}' \tag{2}$$

DOI: 10.1002/fld

energy equation:

$$\rho_\infty c_p \left(\frac{\partial T'}{\partial t'} + \mathbf{u}' \cdot \nabla T' \right) = \alpha \Delta T' \tag{3}$$

where ρ_∞ is the reference density, μ the dynamic viscosity, c_p the specific heat at constant pressure, $\mathbf{g}'$ the gravity force, β' the coefficient of thermal expansion and α the thermal diffusivity coefficient. Equations (1)–(3) can be rewritten in dimensionless form by introducing the following variables:

$$\mathbf{x} = \frac{\mathbf{x}'}{x_\infty}, \quad t = \frac{\alpha t'}{x_\infty^2}, \quad \mathbf{u} = \frac{x_\infty \mathbf{u}'}{\alpha}, \quad p = \frac{x_\infty^2 p'}{\rho_\infty \alpha^2}$$

$$\mathbf{g} = \frac{x_\infty \mathbf{g}'}{\alpha^2}, \quad T = \frac{T' - T_\infty}{T_\mathrm{H} - T_\mathrm{C}}, \quad \beta = \beta'(T_\mathrm{H} - T_\mathrm{C})$$

where the subscript '∞' indicates the reference quantities. We also define the kinematic viscosity v, the Reynolds number Re, the Prandtl number Pr and the Rayleigh number Ra as

$$v = \frac{\mu}{\rho_\infty}, \quad Re = \frac{u_\infty x_\infty}{v}, \quad Pr = \frac{v}{\alpha}, \quad Ra = Pr \, \frac{|\mathbf{g}'| \beta' (T'_\mathrm{H} - T'_\mathrm{C}) x_\infty^3}{v^2} \tag{4}$$

Hence, for natural convection, Equations (1)–(3) can be rewritten in non-dimensionless transport form as

$$\begin{gathered} \nabla \cdot \mathbf{u} = 0 \\ \frac{\mathrm{D}\mathbf{u}}{\mathrm{D}t} + \nabla p - Pr \Delta \mathbf{u} = Pr \, Ra \, T \mathbf{e} \\ \frac{\mathrm{D}T}{\mathrm{D}t} - \Delta T = 0 \end{gathered} \tag{5}$$

For mixed convection, an analogous dimensionalization of Equations (1)–(3) gives

$$\begin{gathered} \nabla \cdot \mathbf{u} = 0 \\ \frac{\mathrm{D}\mathbf{u}}{\mathrm{D}t} + \nabla p - \frac{1}{Re} \Delta \mathbf{u} = T \mathbf{e} \\ \frac{\mathrm{D}T}{\mathrm{D}t} - \frac{1}{Pr \, Re} \Delta T = 0 \end{gathered} \tag{6}$$

In (5) and (6), $\mathbf{e} = (0, 1)^\mathrm{T}$ is the unit vector in direction of gravity and $\mathrm{D}w/\mathrm{D}t$ is the material derivative of any physical variable w defined by

$$\frac{\mathrm{D}w}{\mathrm{D}t} = \frac{\partial w}{\partial t} + \mathbf{u} \cdot \nabla w \tag{7}$$

Note that the coupling in (5) involves the Rayleigh number Ra for natural convection, while the coupling in (6) involves the Reynolds number Re for mixed convection. The Rayleigh and Reynolds numbers, which are the parameters of interest, are usually used to measure the relative importance of convection compared with diffusion in Equations (5) and (6).

DOI: 10.1002/fld

Boundary and initial conditions have to be inserted in Equations (5) and (6) to provide a well-posed mathematical problem. They strongly depend on the problem under consideration. For instance, in most natural convection problems, no-slip boundary conditions are applied for the velocity field, Dirichlet boundary conditions at hot and cold regions on the boundary, and Neumann boundary conditions on the adiabatic regions, i.e.

$$\begin{aligned} \mathbf{u} &= \mathbf{0} \quad \text{on } \Gamma \\ T &= T_{\mathrm{D}} \quad \text{on } \Gamma_{\mathrm{D}} \\ \mathbf{n}\cdot\nabla T &= 0 \quad \text{on } \Gamma_{\mathrm{N}} \end{aligned} \tag{8}$$

where $\mathbf{n}$ is the unit outward normal on the boundary, Γ_{D} and Γ_{N} are the portions of the boundary $\Gamma = \Gamma_{\mathrm{D}} \cup \Gamma_{\mathrm{N}}$ subjected to Dirichlet and Neumann boundary conditions, respectively. Here, $T_{\mathrm{D}} = T_{\mathrm{C}}$ at the cold region of Γ_{D} and $T_{\mathrm{D}} = T_{\mathrm{H}}$ at the hot region of Γ_{D}. Notice that, other boundary conditions for natural and mixed convection can be also incorporated in our formulation without major conceptual modifications.

3. GALERKIN-CHARACTERISTIC METHOD

The emphasis in the current work is on the characteristic treatment of convection. This can be accomplished within the framework of time-splitting schemes for time-dependent problems. Therefore, the proposed Galerkin-characteristic method is described for time-dependent problems even though, it may only be used as a means of reaching the steady-state solution. The temporal accuracy of the method depends on the discretization of the characteristic curves as well as the temporal discretization of the governing equations. Here, we consider second-order schemes for both discretizations. In addition, we formulate our Galerkin-characteristic method only for the natural convection equations (5) and its application to the mixed convection problem (6) is straightforward.

The numerical method we propose for approximating solutions to Equations (5) can be interpreted as a fractional step technique where the convective part is decoupled from the Stokes/Boussinesq part in the temporal discretization. Thus, at each time step the new velocity, temperature and pressure are updated by solving the convection equations

$$\begin{aligned} \frac{\partial \mathbf{u}}{\partial t} + \mathbf{u}\cdot\nabla\mathbf{u} &= \mathbf{0} \\ \frac{\partial T}{\partial t} + \mathbf{u}\cdot\nabla T &= 0 \end{aligned} \tag{9}$$

then the Stokes/Boussinesq equations

$$\begin{aligned} \nabla\cdot\mathbf{u} &= 0 \\ \frac{\partial \mathbf{u}}{\partial t} + \nabla p - Pr\Delta\mathbf{u} &= Pr\,Ra\,T\mathbf{e} \\ \frac{\partial T}{\partial t} - \Delta T &= 0 \end{aligned} \tag{10}$$

DOI: 10.1002/fld

Note that the energy equation in (10) has been decoupled from the momentum equation, which can be solved separately once the convective step (9) is approximated.

In order to formulate our method we require a discretization of the space domain $\bar{\Omega}=\Omega\cup\Gamma$. To perform this step, we proceed as follows. Given h_0, $0<h_0<1$, let h be a space discretization parameter such that $0<h<h_0$. We generate a quasi-uniform partition $\Omega_h\subset\bar{\Omega}$ of small elements $\mathscr{K}_j$ that satisfy the following conditions:

(i) $\bar{\Omega}=\bigcup_{j=1}^{\mathrm{Ne}}\mathscr{K}_j$, where Ne is the number of elements of Ω_h.
(ii) If $\mathscr{K}_i$ and $\mathscr{K}_j$ are two different elements of Ω_h, then

$$\mathscr{K}_i\cap\mathscr{K}_j=\begin{cases}P_{ij} & \text{a mesh point, or}\\ \Gamma_{ij} & \text{a common side, or}\\ \emptyset & \text{empty set}\end{cases}$$

(iii) There exists a positive constant k such that for all $j\in\{1,\ldots,Ne\}$, $d_j/h_j>k$ $(h_j\leqslant h)$, where d_j is the diameter of the circle inscribed in $\mathscr{K}_j$ and h_j is the largest side of $\mathscr{K}_j$.

The conforming finite element spaces for velocity/temperature and pressure that we use are Taylor–Hood finite elements P_m/P_{m-1} (or Q_m/Q_{m-1}), i.e. polynomial of degree $m\geqslant 2$ for the velocity/temperature and polynomial of degree $m-1$ for the pressure on simplices (or quadrilaterals), respectively. It is known that for such elements the discrete velocity/temperature and pressure fields satisfy the inf–sup condition. This property guarantees the stability and convergence of the approximate solutions, compare [13, 14]. These elements can be defined as

$$\mathbf{v}_h=\{\mathbf{u}_h\in\mathbf{C}^0(\bar{\Omega})\colon\ \mathbf{u}_h|_{\mathscr{K}_j}\in S(\mathscr{K}_j)\times S(\mathscr{K}_j),\ \forall\mathscr{K}_j\in\Omega_h\}$$

$$V_h=\{T_h\in C^0(\bar{\Omega})\colon\ T_h|_{\mathscr{K}_j}\in S(\mathscr{K}_j),\ \forall\mathscr{K}_j\in\Omega_h\}$$

$$S_h=\{p_h\in C^0(\bar{\Omega})\colon\ p_h|_{\mathscr{K}_j}\in R(\mathscr{K}_j),\ \forall\mathscr{K}_j\in\Omega_h\}$$

where $S(\mathscr{K}_j)$ and $R(\mathscr{K}_j)$ are polynomial spaces defined in $\mathscr{K}_j$ as $S(\mathscr{K}_j)=P_m(\mathscr{K}_j)$ for simplices, $S(\mathscr{K}_j)=Q_m(\mathscr{K}_j)$ for quadrilaterals, $R(\mathscr{K}_j)=P_{m-1}(\mathscr{K}_j)$ for simplices and $R(\mathscr{K}_j)=Q_{m-1}(\mathscr{K}_j)$ for quadrilaterals.

Next, we discretize the time interval into subintervals $[t_n,t_{n+1}]$ with length Δt and $t_n=n\Delta t$. We use the notation w^n to denote the value of a generic function w at time t_n. Hence, we formulate the finite element solutions to $\mathbf{u}^n(\mathbf{x})$, $T^n(\mathbf{x})$ and $p^n(\mathbf{x})$ as

$$\mathbf{u}_h^n(\mathbf{x})=\sum_{j=1}^{M}U_j^n\phi_j(\mathbf{x}),\quad T_h^n(\mathbf{x})=\sum_{j=1}^{M}\mathscr{T}_j^n\phi_j(\mathbf{x}),\quad p_h^n(\mathbf{x})=\sum_{j=1}^{N}P_j^n\psi_j(\mathbf{x}) \tag{11}$$

where M and N are, respectively, the number of velocity/temperature and pressure mesh points in the partition Ω_h. The functions U_j^n, $\mathscr{T}_j^n$ and P_j^n are the corresponding nodal values of $\mathbf{u}_h^n(\mathbf{x})$, $T_h^n(\mathbf{x})$ and $p_h^n(\mathbf{x})$, respectively. They are defined as $U_j^n=\mathbf{u}_h^n(\mathbf{x}_j)$, $\mathscr{T}_j^n=T_h^n(\mathbf{x}_j)$ and $P_j^n=p_h^n(\mathbf{y}_j)$, where $\{\mathbf{x}_j\}_{j=1}^M$ and $\{\mathbf{y}_j\}_{j=1}^N$ are the set of velocity/temperature and pressure mesh points in the partition Ω_h, respectively, so that $N<M$ and $\{\mathbf{y}_1,\ldots,\mathbf{y}_N\}\subset\{\mathbf{x}_1,\ldots,\mathbf{x}_M\}$. In (11), $\{\phi_j\}_{j=1}^M$ and $\{\psi_j\}_{j=1}^N$ are the set of global nodal basis functions of $\mathbf{v}_h$ and S_h, respectively, characterized by the property $\phi_i(\mathbf{x}_j)=\delta_{ij}$ and $\psi_i(\mathbf{y}_j)=\delta_{ij}$ with δ_{ij} denoting the Kronecker symbol.

DOI: 10.1002/fld

3.1. The convection fractional step

To solve the convection equations (9) two steps are required, namely the computation of characteristic trajectories and the interpolation procedure. Both steps are crucial to the overall accuracy of Galerkin-characteristic methods. For each mesh point $\mathbf{x}_j$, $j=1,\ldots,M$, the characteristic curves $\mathbf{X}_{hj}^n=\mathbf{X}_h(\mathbf{x}_j,t_{n+1};t_n)$ associated with (7) are the unique solutions of the ordinary differential equation

$$\begin{aligned}\frac{\mathrm{d}\mathbf{X}_h(\mathbf{x}_j,t_{n+1};t)}{\mathrm{d}t}&=\mathbf{u}_h(t,\mathbf{X}_h(\mathbf{x}_j,t_{n+1};t))\\ \mathbf{X}_h(\mathbf{x}_j,t_{n+1};t_{n+1})&=\mathbf{x}_j\end{aligned}\tag{12}$$

where $\mathbf{u}_h(t,\mathbf{x})$ is the approximate flow velocity at time t. The solutions of (12) are known by departure points at time t of a fluid particle passing through the point $\mathbf{x}_j$ at time $t=t_{n+1}$. To compute the departure points $\{\mathbf{X}_{hj}^n\}$, $j=1,\ldots,M$, we use the algorithm proposed by Temperton and Staniforth [1] together with an efficient search-locate algorithm developed by Allievi and Bermejo [15]. The first algorithm accurately solves (12) with a second-order scheme in unstructured meshes, while the second algorithm efficiently identifies the mesh element of Ω_h where the departure point is located.

Let us write the solution of (12) as

$$\mathbf{X}_{hj}^n=\mathbf{x}_j-\alpha_{hj}\tag{13}$$

where the displacement α_{hj} is calculated by the iterative procedure

$$\alpha_{hj}^{(k+1)}=\frac{\Delta t}{2}\left[3\mathbf{u}_h^n\left(\mathbf{x}_j-\frac{1}{2}\,\alpha_{hj}^{(k)}\right)-\mathbf{u}_h^{n-1}\left(\mathbf{x}_j-\frac{1}{2}\,\alpha_{hj}^{(k)}\right)\right],\quad k=0,1,\ldots\tag{14}$$

with

$$\alpha_{hj}^{(0)}=\frac{\Delta t}{2}[3\mathbf{u}_h^n(\mathbf{x}_j)-\mathbf{u}_h^{n-1}(\mathbf{x}_j)]$$

To compute the velocity values $\mathbf{u}_h^n(\mathbf{x}_j-\frac{1}{2}\,\alpha_{hj}^{(k)})$ and $\mathbf{u}_h^{n-1}(\mathbf{x}_j-\frac{1}{2}\,\alpha_{hj}^{(k)})$ we first identify, using the search-locate algorithm, the mesh element $\hat{\mathscr{K}}_j$ where $\mathbf{x}_j-\frac{1}{2}\,\alpha_{hj}^{(k)}$ resides. Then a finite element interpolation on $\hat{\mathscr{K}}_j$ is carried out according to (11). In our numerical results, the iterations in (14) were continued until the trajectory changed by less than 10^{-5}. However, in practice it is not recommended to repeat the iteration process more than a few times due to efficiency considerations.

Assuming that, for all $j=1,\ldots,M$, the pairs $(\mathbf{X}_{hj}^n,\hat{\mathscr{K}}_j)$ and the mesh point values $\{U_j^n,\mathscr{T}_j^n\}$ are known, we compute the values $\{\hat{U}_j^n,\hat{\mathscr{T}}_j^n\}$ as

$$\hat{U}_j^n:=\mathbf{u}_h^n(\mathbf{X}_{hj}^n)=\sum_{k=1}^M U_k\phi_k(\mathbf{X}_{hj}^n),\quad \hat{\mathscr{T}}_j^n:=T_h^n(\mathbf{X}_{hj}^n)=\sum_{k=1}^M \mathscr{T}_k\phi_k(\mathbf{X}_{hj}^n)\tag{15}$$

Then, the solution $\{\hat{\mathbf{u}}_h^n(\mathbf{x}),\hat{T}_h^n(\mathbf{x})\}$ of the convection equations (9) is obtained as

$$\hat{\mathbf{u}}_h^n(\mathbf{x})=\sum_{j=1}^M \hat{U}_j^n\phi_j(\mathbf{x}),\quad \hat{T}_h^n(\mathbf{x})=\sum_{j=1}^M \hat{\mathscr{T}}_j^n\phi_j(\mathbf{x})\tag{16}$$

DOI: 10.1002/fld

The above convection fractional step follows the flow by tracking the characteristics backward from a point $\mathbf{x}$ in a fixed grid at the time step t_{n+1} to a point $\mathbf{X}$ at the previous time step t_n. Hence, the present procedure avoids the grid distortion problems present in forward tracking methods. We should mention that the conventional Galerkin-characteristic methods in [2, 3] suggest the evaluation of $\hat{\mathbf{u}}_h^n$ and $\hat{T}_h^n$ in (16) using an L^2-projection on the space of the velocity $\mathbf{v}_h$ and of temperature V_h, respectively. In many applications, the evaluation of integrals in the L^2-projection is difficult and computationally very demanding. An alternative approach was studied in [4] for convection–diffusion problems and was recently proposed by Seaïd and El-Amrani [16] for the shallow water equations.

3.2. The Stokes/Boussinesq fractional step

To perform the Stokes/Boussinesq step (10) we present a projection-type method and a direct-type method. In both methods, the time integration is carried out using a second-order θ-scheme. First, we formulate the projection-type method.

3.2.1. Galerkin-characteristic projection (GCPR) scheme. The procedure to advance the solution of (10) from a time t_n to the next time t_{n+1} can be carried out in the following steps:

1. Solve for T^{n+1}

$$\begin{aligned} \frac{T^{n+1}-\hat{T}^n}{\Delta t}-\Delta T^{n+\theta}&=0 \quad \text{in } \Omega \\ T^{n+1}&=T_{\mathrm{D}} \quad \text{on } \Gamma_{\mathrm{D}} \\ \mathbf{n}\cdot\nabla T^{n+1}&=0 \quad \text{on } \Gamma_{\mathrm{N}} \end{aligned} \tag{17}$$

2. Solve for $\bar{\mathbf{u}}^{n+1}$

$$\begin{aligned} \frac{\bar{\mathbf{u}}^{n+1}-\hat{\mathbf{u}}^n}{\Delta t}+\gamma\nabla p^n-Pr\Delta\bar{\mathbf{u}}^{n+\theta}&=Pr\,Ra\,T^{n+1}\mathbf{e} \quad \text{in } \Omega \\ \bar{\mathbf{u}}^{n+1}&=\mathbf{0} \quad \text{on } \Gamma \end{aligned} \tag{18}$$

3. Solve for $\bar{p}$ and $\mathbf{u}^{n+1}$

$$\begin{aligned} \frac{\mathbf{u}^{n+1}-\bar{\mathbf{u}}^{n+1}}{\Delta t}+\nabla\bar{p}&=\mathbf{0} \quad \text{in } \Omega \\ \nabla\cdot\mathbf{u}^{n+1}&=0 \quad \text{in } \Omega \\ \mathbf{n}\cdot\nabla\mathbf{u}^{n+1}&=0 \quad \text{on } \Gamma \end{aligned} \tag{19}$$

4. Update p^{n+1}

$$p^{n+1}=\gamma p^n+(1+\gamma)\bar{p}$$

In (17) and (18), $T^{n+\theta}$ and $\bar{\mathbf{u}}^{n+\theta}$ are defined as

$$T^{n+\theta}=\theta T^{n+1}+(1-\theta)\hat{T}^n, \quad \bar{\mathbf{u}}^{n+\theta}=\theta\bar{\mathbf{u}}^{n+1}+(1-\theta)\hat{\mathbf{u}}^n$$

DOI: 10.1002/fld

with θ and γ are fixed parameter in $[0, 1]$. In our computations, we used $\theta = \frac{1}{2}$ and $\gamma = 1$. Note that, the solution of (19) leads to a pressure-Poisson problem for $\bar{p}$ of the form

$$\begin{aligned} \Delta \bar{p} &= \frac{1}{\Delta t} \nabla \cdot \bar{\mathbf{u}}^{n+1} \quad \text{in } \Omega \\ \mathbf{n} \cdot \nabla \bar{p} &= 0 \qquad\qquad\quad \text{on } \Gamma \end{aligned} \tag{20}$$

Note that no outer iterations are required to compute the solution in the GCPR method within a time step. Another option is to solve the full Stokes/Boussinesq problem (10) for velocity/temperature and pressure directly at each time step using a conjugate-gradient method. This direct-type procedure can be viewed as a penalty method. It involves outer iterations and has the ability to enforce exactly the divergence-free constraint for finite values of penalty parameter, compare [8, 17]. Its formulation is given below.

3.2.2. Galerkin-characteristic conjugate gradient (GCCG) scheme. Given a tolerance ε and using superscripts in parenthesis to indicate the iteration numbers, the GCCG algorithm is carried out in the following steps:

1. Solve for $T_h^{n+1} \in V_h$ such that for all $v_h \in V_h^0$

$$\frac{1}{\Delta t} \int T_h^{n+1} v_h \, \mathrm{d}\Omega + \frac{1}{2} \int \nabla T_h^{n+1} \cdot \nabla v_h \, \mathrm{d}\Omega = \frac{1}{\Delta t} \int \hat{T}_h^n v_h \, \mathrm{d}\Omega - \frac{1}{2} \int \nabla \hat{T}_h^n \cdot \nabla v_h \, \mathrm{d}\Omega \tag{21}$$

subject to boundary conditions

$$\begin{aligned} T_h^{n+1} &= T_{\mathrm{D}} \quad \text{on } \Gamma_{\mathrm{D}} \\ \mathbf{n} \cdot \nabla T_h^{n+1} &= 0 \quad \text{on } \Gamma_{\mathrm{N}} \end{aligned}$$

2. Given $p_h^{(0)} = p_h^n$, solve for $\mathbf{u}_h^{(0)} \in \mathbf{v}_h$ such that for all $\mathbf{v}_h \in \mathbf{v}_h^0$

$$\begin{aligned} \frac{1}{\Delta t} \int \mathbf{u}_h^{(0)} \mathbf{v}_h \, \mathrm{d}\Omega + \frac{Pr}{2} \int \nabla \mathbf{u}_h^{(0)} \cdot \nabla \mathbf{v}_h \, \mathrm{d}\Omega &= \frac{1}{\Delta t} \int \hat{\mathbf{u}}_h^n \mathbf{v}_h \, \mathrm{d}\Omega \\ &\quad - \frac{Pr}{2} \int \nabla \hat{\mathbf{u}}_h^n \cdot \nabla \mathbf{v}_h \, \mathrm{d}\Omega + \int p_h^{(0)} \nabla \cdot \mathbf{v}_h \, \mathrm{d}\Omega \\ &\quad + \frac{Pr\,Ra}{2} \int (T_h^{n+1} + \hat{T}_h^n) \mathbf{v}_h \cdot \mathbf{e} \, \mathrm{d}\Omega \end{aligned} \tag{22}$$

subject to boundary conditions

$$\mathbf{u}_h^{(0)} = \mathbf{0} \quad \text{on } \Gamma$$

Then, compute

$$r_h^{(0)} = \nabla \cdot \mathbf{u}_h^{(0)}$$

3. Solve for $\psi_h^{(0)} \in S_h$ such that for all $\phi_h \in S_h$

$$\int_\Omega \nabla \psi_h^{(0)} \cdot \nabla \phi_h \, \mathrm{d}\Omega = \int_\Omega r_h^{(0)} \phi_h \, \mathrm{d}\Omega$$

DOI: 10.1002/fld

and set

$$g_h^{(0)} = \frac{1}{\Delta t}\,\psi_h^{(0)} + \frac{Pr}{2}\,r_h^{(0)}, \quad \omega_h^{(0)} = g_h^{(0)}$$

For $m \geqslant 0$, assume that $p_h^{(m)}$, $\mathbf{u}_h^{(m)}$, $r_h^{(m)}$, $g_h^{(m)}$, $w_h^{(m)}$ are known, we compute $p_h^{(m+1)}$, $\mathbf{u}_h^{(m+1)}$, $r_h^{(m+1)}$, $g_h^{(m+1)}$ and $w_h^{(m+1)}$ as follows:

(a) Solve for $\bar{\mathbf{u}}_h \in \mathbf{v}_h^0$ such that for all $\mathbf{v}_h \in \mathbf{v}_h^0$

$$\frac{1}{\Delta t}\int \bar{\mathbf{u}}_h^{(m)}\mathbf{v}_h\,\mathrm{d}\Omega + \frac{Pr}{2}\int \nabla\bar{\mathbf{u}}_h^{(m)} \cdot \nabla\mathbf{v}_h\,\mathrm{d}\Omega = \int \omega_h^{(m)}\nabla\cdot\mathbf{v}_h\,\mathrm{d}\Omega \tag{23}$$

and set

$$\bar{r}_h^{(m)} = \nabla\cdot\bar{\mathbf{u}}_h^{(m)}$$

(b) Compute

$$\rho_m = \frac{\int r_h^{(m)} g_h^{(m)}\,\mathrm{d}\Omega}{\int \bar{r}_h^{(m)}\omega_h^{(m)}\,\mathrm{d}\Omega}$$

(c) Set

$$p_h^{(m+1)} = p_h^{(m)} - \rho_m\omega_h^{(m)}$$

$$\mathbf{u}_h^{(m+1)} = \mathbf{u}_h^{(m)} - \rho_m\bar{\mathbf{u}}_h^{(m)}$$

$$r_h^{(m+1)} = r_h^{(m)} - \rho_m\bar{r}_h^{(m)}$$

(d) Solve for $\bar{\psi}_h^{(k)} \in S_h$ such that for all $\phi_h \in S_h$

$$\int \nabla\bar{\psi}_h^{(m)} \cdot \nabla\phi_h\,\mathrm{d}\Omega = \int \bar{r}_h^{(m)}\phi_h\,\mathrm{d}\Omega$$

and set

$$g_h^{(m+1)} = g_h^{(m)} - \rho_m\left(\frac{1}{\Delta t}\,\psi_h^{(m)} + \frac{Pr}{2}\,r_h^{(m)}\right)$$

i. If $\int r_h^{(m+1)} g_h^{(m+1)}\,\mathrm{d}\Omega / \int r_h^{(0)} g_h^{(0)}\,\mathrm{d}\Omega \leqslant \varepsilon$
then

$$p_h^{n+1} = p_h^{(m+1)}, \quad \mathbf{u}_h^{n+1} = \mathbf{u}_h^{(m+1)}$$

stop.

DOI: 10.1002/fld

ii. Else, compute

$$\eta_m = \frac{\int r_h^{(m+1)} g_h^{(m+1)} \, d\Omega}{\int r_h^{(m)} g_h^{(m)} \, d\Omega}, \quad \omega_h^{(m+1)} = g_h^{(m+1)} + \eta_m \omega_h^{(m)}$$

change $m \longleftarrow m+1$, return to step (a) and repeat.

iii. End if

It is noteworthy that the finite element discretization of Equations (17)–(23) is trivial and is omitted here. It is described in many text books, compare [18] among others.

4. NUMERICAL RESULTS

We present numerical results for two benchmark problems in natural convection and mixed convection. The main goals of this section are to illustrate the numerical performance of the Galerkin-characteristic algorithms described above and to verify numerically their capabilities to solve natural and mixed convection problems. In all the computations reported herein, unless specified, the time step Δt is fixed to 0.1 and all the linear systems of algebraic equations are solved using the conjugate gradient solver with incomplete Cholesky decomposition (ICCG). In addition, all stopping criteria for iterative solvers were set to 10^{-5}, which is small enough to guarantee that the algorithm truncation error dominated the total numerical error. In our Galerkin-characteristic algorithms, the number of iterations to reach this tolerance do not overpass 15 iterations for the velocity/temperature and 40 iterations for the Poisson problems for the pressure in both natural and mixed convection problems. We should note that the conjugate gradient ICCG solver for linear systems and GCCG method are completely different.

For comparison reasons, we compare the results obtained using our Galerkin-characteristic algorithms to those obtained using Eulerian-based Galerkin finite element methods widely used in the literature to solve incompressible Navier–Stokes equations in primitive variables. Hereafter, we shall use the terminology GCCG, GCPR, EGPR, EGS2 and EGS3 to refer to Galerlin-characteristic conjugate gradient method, Galerlin-characteristic projection method, Eulerian-based projection method, Eulerian-based Galerkin splitting with two stages and Eulerian-based Galerkin splitting with three stages, respectively. For completeness, a brief formulation of EGPR, EGS2 and EGS3 methods is given in the Appendix.

All the computations are made on a Pentium PC with one processor of 518 MB of RAM and 166 MHz. The codes only take the default optimization of the machine, i.e. they are not parallel codes.

4.1. Natural convection in a squared cavity

We consider the canonical problem of buoyancy-driven flow in a squared cavity with vertical side walls differentially heated. The flow domain $\Omega = [0, 1] \times [0, 1]$ with the left and right vertical walls are maintained at fixed temperatures $T = T_H$ and $T = T_C$, respectively. The bottom and top horizontal walls are adiabatic. No-slip boundary conditions are imposed for the fluid flow at all walls. The literature is abundant for this natural convection flow which shows thermal phenomena at many scales depending on *Ra* numbers, see for example [19–21]. The local Nusselt number at

DOI: 10.1002/fld

Table I. Spatial error-norms for the natural convection at time $t = 300$.

		Errors in T			Errors in u		
Ra	h	L^∞-error	L^1-error	L^2-error	L^∞-error	L^1-error	L^2-error
10^3	1/32	0.10781E−00	0.93110E−01	0.97201E−01	0.16976E−00	0.11053E−00	0.13964E−00
	1/64	0.29087E−01	0.23931E−01	0.25508E−01	0.46764E−01	0.28805E−01	0.36900E−01
	1/128	0.73225E−02	0.58598E−02	0.63329E−02	0.11936E−01	0.71517E−02	0.92251E−02
	1/256	0.17560E−02	0.13574E−02	0.14874E−02	0.29228E−02	0.16798E−02	0.22277E−02
10^7	1/32	0.11390E−00	0.10322E−00	0.10975E−00	0.19205E−00	0.13861E−00	0.17702E−00
	1/64	0.31814E−01	0.28043E−01	0.30233E−01	0.54016E−01	0.38183E−01	0.49445E−01
	1/128	0.81208E−02	0.70595E−02	0.76638E−02	0.13883E−02	0.96791E−02	0.12621E−02
	1/256	0.20302E−02	0.17285E−02	0.19027E−02	0.34709E−02	0.23864E−02	0.31334E−02

the hot wall Nu_H and the cold wall Nu_C are calculated as

$$Nu_H = -\left.\frac{\partial T}{\partial x}\right|_{\text{heated wall}} \quad \text{and} \quad Nu_C = -\left.\frac{\partial T}{\partial x}\right|_{\text{cold wall}}$$

The main issues we wish to address in this example are concerned with the capabilities of the GCCG scheme to accurately approximate numerical solutions to this well-established test problem. The efficiency of the GCCG scheme is also examined by comparing the computational work of the obtained simulations with those obtained using the GCPR, EGPR, EGS2 and EGS3 methods. First, we examine the grid convergence in the GCCG scheme for the proposed model. To this end, we report in Table I the relative spatial error-norms varying in the mesh size h and keeping Δt fixed. All the errors are measured by the difference between the pointvalues of the reference solution and the reconstructed pointvalues of the computed solutions. The reference solution corresponds to the solution obtained by the GCCG scheme in the fine mesh with $h = \frac{1}{512}$. As expected, for the two selected Ra numbers, the error-norms decay as the mesh size h decreases. A slow decay rate has been detected in the error-norms for the velocity variable. It is clear that the GCCG scheme shows a second-order behaviour in space for the considered natural convection.

To check the grid independence of solutions in the GCCG scheme we display in Figure 1 the local Nusselt number at the hot wall obtained for different mesh levels. We have observed that for low Ra numbers, the grid independence in the computed solution is achieved on meshes which are coarser than those required for high Ra numbers. It is easy to verify that for the last two mesh levels the differences in error-norms reported in Table I and the plots in Figure 1 are always very small. These results ensure grid independence of the numerical results. Hence, our next computations are realized with a structured triangulation P_2/P_1 with 12 800 elements and $h = 1/160$. Flow and temperature fields in the cavity and Nusselt numbers are examined for ranges of Rayleigh number from 10^3 to 10^8 with a Prandtl number $Pr = 0.71$.

In Figure 2, we display the isotherms, vorticity contours, velocity vectors, and streamlines obtained using the GCCG method for different Rayleigh numbers at time $t = 300$. At this time, the flow has all the characteristic features of the steady state. As can be seen, the flow is symmetric with respect to the cavity centre for all the Rayleigh numbers. At low Ra numbers, the flow exhibits a central vortex and the heat transfer is dominated by conduction regime. At $Ra = 10^5$, the vortex breaks into two vortices moving towards the vertical walls. At high Rayleigh numbers, the

DOI: 10.1002/fld

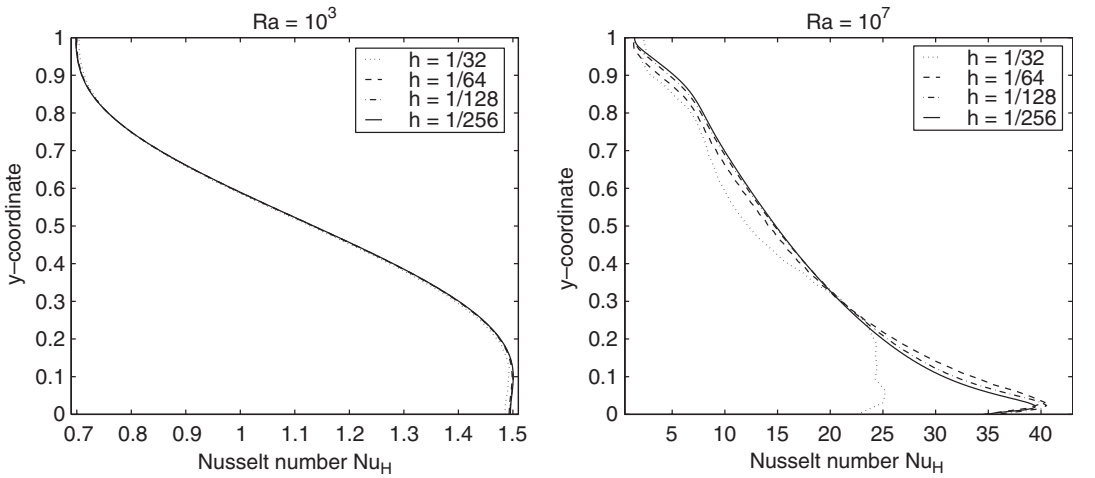

Figure 1. Local Nusselt number at the hot wall, Nu_{H}, at different mesh levels for $Ra = 10^3$ (left plot) and $Ra = 10^7$ (right plot).

flow becomes fully convection dominated, the cold fluid is entrained right to the hot wall where high-temperature gradients are created. There is excellent agreement between these results and those published in [19–21]. Note that the performance of our GCCG method is very attractive since the computed solutions remain stable and highly accurate even when coarse meshes are used without solving non-linear problems or requiring special projection or pressure correction procedures.

The u-velocity component along the vertical and the v-velocity component along the horizontal centre lines are shown in Figure 3 for all the values of Rayleigh numbers. A cross-section of the temperature at the horizontal centre line is shown in Figure 4. The boundary layers for the velocity components and temperature field can be observed clearly. As expected, the velocity and temperature profiles change from curved at lower values of Ra to linear for higher Ra values. These results agree well with those from previous studies in [19–21].

Figure 5 presents the distribution of the local Nusselt number at the cold wall. The distribution of the local Nusselt number at the hot wall is shown in Figure 6. The features of distribution at low Rayleigh numbers differ from that at high Rayleigh numbers. We observe that, the rate of heat transfer from the wall to the fluid, and *vice versa*, increases with the Rayleigh number. At low Rayleigh number, conduction heat transfer dominates and the heat transfer rate from the walls is very little. The maximum local Nusselt number is located at the bottom of the hot wall and minimum at the top wall. At the cold wall, the minimum local Nusselt number is located at the bottom and maximum at the top wall. Similar aspects have been reported in References [19–21]. Furthermore, to quantitatively assess the accuracy of the GCCG method, we display in Table II comparisons between published results for maximum horizontal velocity at the cavity mid-width and results obtained with our GCCG method. The obtained results for vertical velocity at the cavity mid-height are listed in Table III. The results mostly agree with all the model results in References [19–21]. As is obvious from the tables, the small difference to other methods can be attributed to the mesh size used in the present investigation.

DOI: 10.1002/fld

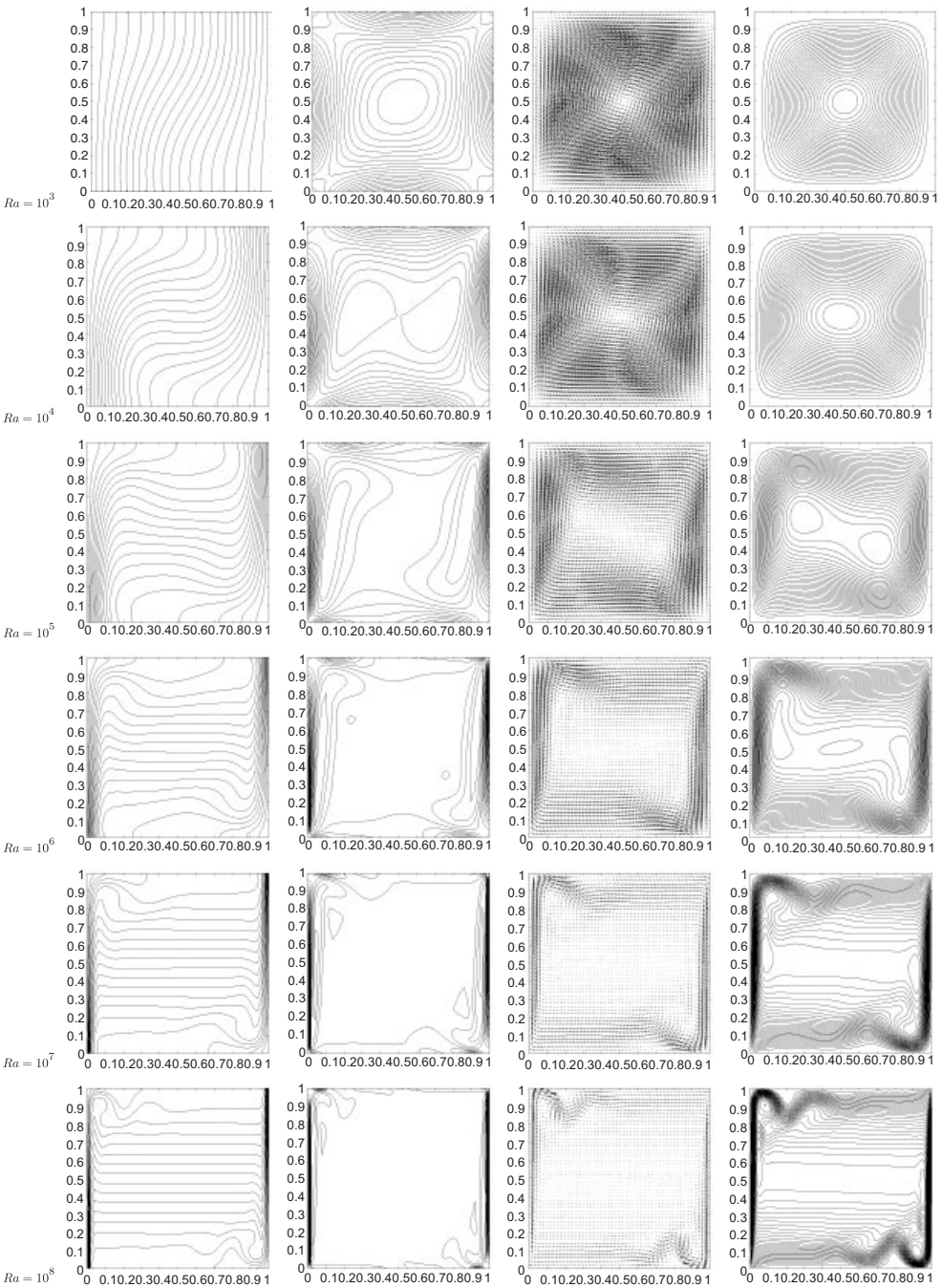

Figure 2. Isothermal lines (first column), vorticity contours (second column), velocity field (third column) and streamlines (fourth column) obtained using GCCG method for the natural convection.

DOI: 10.1002/fld

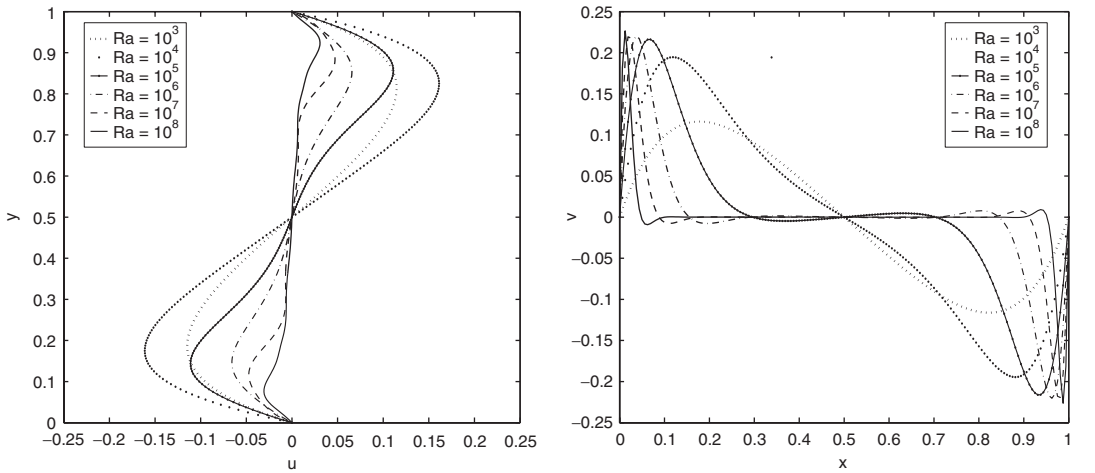

Figure 3. Variation of u-velocity at $x = 0.5$ (left plot) and v-velocity at $y = 0.5$ (right plot).

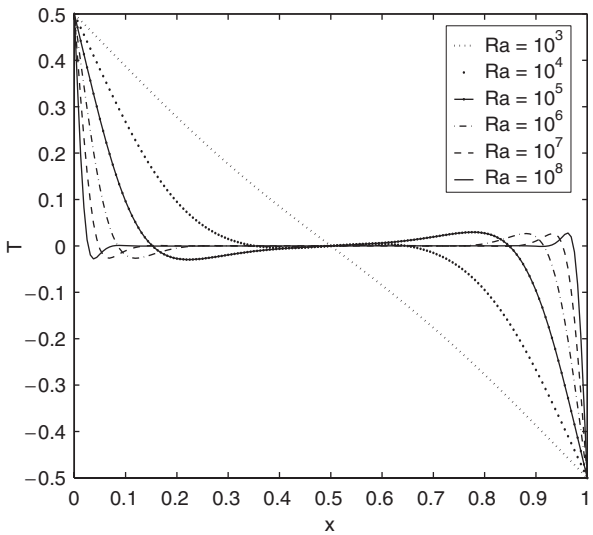

Figure 4. Variation of temperature at mid-height cavity $y = 0.5$.

In order to quantify the GCCG results we summarize in Table IV maximum and minimum of Nusselt number at the hot wall Nu_{H}, u and v velocities. The results obtained using the other methods are also included in this table. As can be seen, GCCG and EGS3 methods produce nearly identical results which compare satisfactorily with those published in [22]. The differences in EGS2 and EGS3 schemes are also modest. However, the simulated results from the EGPR scheme and the GCPR scheme are worse than those of the GCCG scheme and the EGS3 scheme, especially the EGPR scheme blows up at high Rayleigh numbers.

DOI: 10.1002/fld

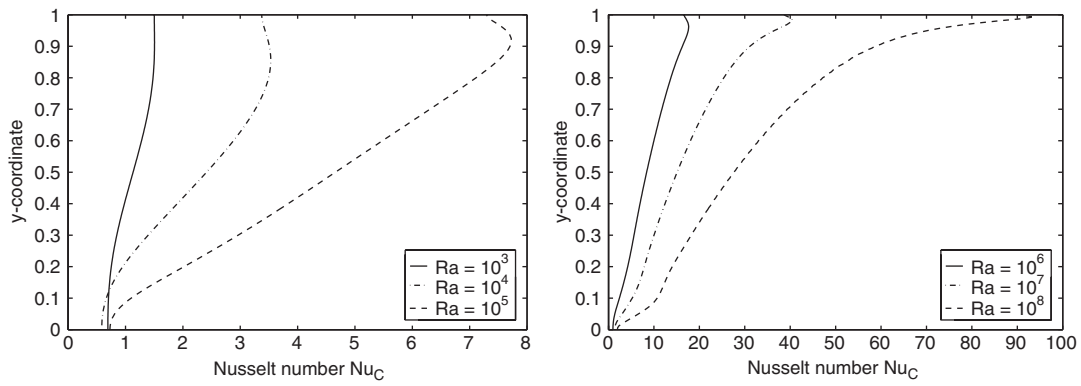

Figure 5. Local Nusselt number at the cold wall, Nu_C, for the natural convection.

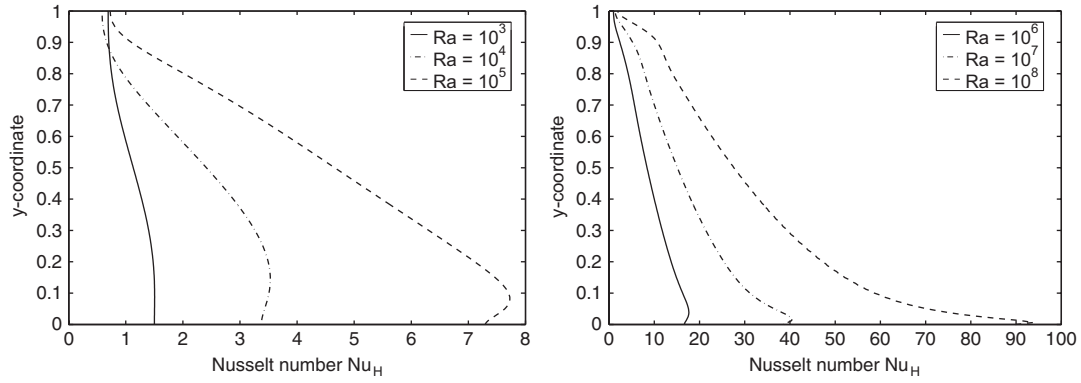

Figure 6. Local Nusselt number at the hot wall, Nu_H, for the natural convection.

Table II. Comparison between published results for maximum horizontal velocity u at the cavity mid-width $x = 0.5$ and results obtained with GCCG method. Number in parenthesis corresponds to the y co-ordinate.

Ra	Reference [19]	Reference [20]	Reference [21]	Present work
10^3	3.634 (0.813)	3.68 (0.817)	3.6493 (0.8125)	3.6450 (0.815)
10^4	16.2 (0.823)	16.1 (0.817)	16.1798 (0.8235)	16.0891 (0.818)
10^5	34.81 (0.855)	34.0 (0.857)	34.7741 (0.8535)	34.0065 (0.851)
10^6	65.33 (0.851)	65.4 (0.875)	64.6912 (0.8460)	65.3390 (0.860)
10^7	NA	139.7 (0.919)	145.2666 (0.8845)	145.0317 (0.905)
10^8	NA	NA	283.689 (0.9455)	292.8106 (0.943)

DOI: 10.1002/fld

Table III. Comparison between published results for maximum vertical velocity v at the cavity mid-height $y = 0.5$ and results obtained with GCCG method. Number in parenthesis corresponds to the x co-ordinate.

Ra	Reference [19]	Reference [20]	Reference [21]	Present work
10^3	3.679 (0.179)	3.73 (0.1827)	3.6962 (0.1790)	3.6981 (0.180)
10^4	19.51 (0.12)	19.9 (0.1246)	19.6177 (0.1195)	19.8955 (0.119)
10^5	68.22 (0.066)	70.0 (0.068)	68.6920 (0.0665)	69.7392 (0.069)
10^6	216.75 (0.0387)	228 (0.039)	220.8331 (0.0380)	226.4970 (0.040)
10^7	NA	698 (0.0235)	703.2536 (0.0215)	707.6305 (0.022)
10^8	NA	NA	2223.4424 (0.013)	2269.7614 (0.013)

Table IV. Comparison of maximum and minimum of Nusselt number at hot wall Nu_H, u and v velocities.

		$\min Nu_H$	$\max Nu_H$	$\min u$	$\min v$	$\max u$	$\max v$
	GCCG	0.6917	1.5055	−0.1152	−0.1168	0.1152	0.1168
	GCPR	0.6982	1.5002	−0.1148	−0.1162	0.1148	0.1162
$Ra = 10^3$	EGS2	0.6915	1.5058	−0.1154	−0.1169	0.1154	0.1169
	EGS3	0.6916	1.5056	−0.1153	−0.1169	0.1153	0.1169
	EGPR	0.6949	1.4976	−0.1156	−0.1170	0.1156	0.1170
	GCCG	0.7485	7.7257	−0.1198	−0.2167	0.1197	0.2167
	GCPR	0.7480	7.6678	−0.1109	−0.2168	0.1109	0.2168
$Ra = 10^5$	EGS2	0.7285	7.7257	−0.1098	−0.2167	0.1098	0.2167
	EGS3	0.7285	7.7258	−0.1098	−0.2167	0.1098	0.2167
	EGPR	0.7259	7.7211	−0.1100	−0.2168	0.1100	0.2168
	GCCG	1.9587	93.8349	−0.0318	−0.2217	0.0318	0.2217
	GCPR	1.8467	91.3337	−0.0299	−0.2263	0.0300	0.2266
$Ra = 10^8$	EGS2	1.9141	93.5674	−0.0318	−0.2217	0.0318	0.2217
	EGS3	1.9586	93.8349	−0.0319	−0.2217	0.0319	0.2217
	EGPR	—	—	—	—	—	—

Our next concern is to ascertain the efficiency of the GCCG scheme. To this end we list in Table V the CPU time for different Ra numbers. Timings, in minutes, include all aspects of computations (grid generation, reconstruction of matrices and solution of linear systems). As clearly shown in the table, for each method, the CPU time increases with Ra number. For a given value of Ra number, the CPU times are comparable for GCCG and EGPR methods. At all Ra numbers, the GCPR scheme performs best, while the EGPR scheme does the best only at low Ra number. However, at high Ra numbers, the EGPR method goes unstable (Tables IV and V corresponds to runs where the EGPR scheme becomes unstable). At $Ra = 10^7$ and 10^8, the CPU time exhibits an increase for all the methods. It is to be remarked that in the GCCG scheme for $Ra = 10^8$, the number of iteration required in the ICCG solver (solver of linear systems) at each time step starts at about 15–10 but it promptly decreases to 2–3, even 1, long before steady state is reached.

DOI: 10.1002/fld

Table V. Comparison of computational times (in minutes) for the natural convection problem.

Ra	GCPR	GCCG	EGPR	EGS2	EGS3
10^3	158	234	272	408	471
10^4	128	180	190	272	325
10^5	111	147	143	210	240
10^6	89	117	125	186	251
10^7	83	115	—	189	295
10^8	98	144	—	286	416

This later behaviour deteriorates in the Eulerian-based methods where the number of iterations in ICCG solver can increase about five times more than in GCCG method.

4.2. Mixed convection past a circular cylinder

To demonstrate the capability of the Galerkin-characteristic methods for a more complex problem, we consider the problem of a viscous thermal flow in a channel containing a circular cylinder. The isothermal version of this example has been the subject of many numerical validations for laminar flows, see for instance [23–25]. Here, a viscous incompressible flow at cold temperature T_C enters through the left boundary of channel with uniform velocity $u_\infty = 1$ while both, the upper and lower, walls are kept at hot temperature T_H. The fluid flows past a circular cylinder with diameter $D = 1$ and also at hot temperature T_H. The Reynolds number for this problem is defined as $Re = Du_\infty/\nu$. At the downstream boundary we impose the pseudo-stress condition

$$\boldsymbol{\tau} := -p\mathbf{n} + \nu \frac{\partial \mathbf{u}}{\partial \mathbf{n}} = \mathbf{0}$$

On the remaining boundaries we use the condition $\mathbf{u} = \mathbf{0}$. A similar test problem has been investigated by Kieft *et al.* [26]. We perform computations with the triangular finite element P_2/P_1 using the unstructured mesh depicted in Figure 7. The mesh contains 2724 triangles resulting in 5628 velocity/temperature nodes and 1452 pressure nodes. Simulations were performed for air ($Pr = 0.71$) at different Reynolds numbers ranging from 20 to 200, above which the wake behind the cylinder becomes unsteady and Karman vortex shedding appears.

In contrast to the previous example where the cavity is bounded by rigid and fixed walls, the considered mixed convection is solved in a open domain. As a consequence, the later flow is more difficult to handle; the results shown here illustrate the robustness of the GCCG method. On the other hand, unlike the previous test example, the mixed convection is a problem unsteady in nature and therefore, good numerical accuracy is required in order to capture the different phenomena present in the evolving solution. This problem is also used to test the accuracy of the GCCG scheme in time. Table VI presents the relative L^2-error in the time interval $(0, T]$ for the temperature and u-velocity variables at $Re = 40$ and 100. The relative L^2-error is defined by

$$\frac{\|w - w_{\text{ref}}\|_{L^2((0,T])}}{\|w_{\text{ref}}\|_{L^2((0,T])}}$$

DOI: 10.1002/fld

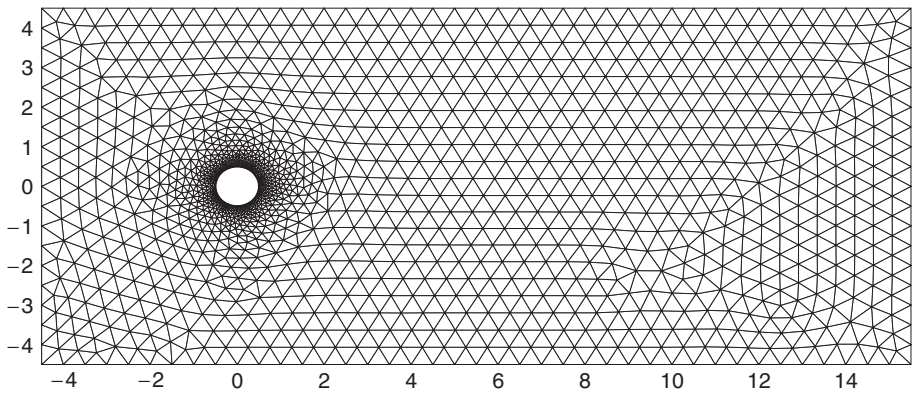

Figure 7. Computational mesh for mixed convection flow past a cylinder.

Table VI. The relative L^2-error for the mixed convection at time $t = 50$.

	$Re = 40$		$Re = 100$	
Δt	Temperature	u-velocity	Temperature	u-velocity
0.1	0.53719E−01	0.79631E−01	0.60695E−01	0.91204E−01
0.05	0.13429E−01	0.20046E−01	0.15279E−01	0.23119E−01
0.025	0.30894E−02	0.47084E−02	0.36642E−02	0.57002E−02
0.0125	0.66774E−03	0.10535E−02	0.80860E−03	0.13204E−02
0.00625	0.11561E−03	0.19961E−03	0.15750E−03	0.27567E−03

where w_{ref} is the reference solution computed by the GCCG scheme on the same mesh using a very small time step of $\Delta t = 0.0005$. The clear indication from Table VI is that the L^2-error decays as the time step Δt decreases. It is evident that the GCCG method reaches the expected second-order accuracy in time. In addition, if instead of computing the approximate convergence rate between two consecutive time refinings, one approximates the convergence rate between time level of $\Delta t = 0.1$ and 0.00625, the results for the temperature variable are 2.21 at $Re = 40$ and 2.14 at $Re = 100$. The results for the u-velocity variable are 2.16 at $Re = 40$ and 2.09 at $Re = 100$. This clearly demonstrates the second-order accuracy of the GCCG algorithm.

In Figure 8, we present the results obtained by the GCCG scheme for different Reynolds numbers. Here, we show the distribution of stream function, pressure, temperature and velocity vectors. The figure indicates circulation zones moving downstream. The results also indicate that as the Re increases, the size of the recirculation zone increases with the flow exhibiting eddies with different magnitudes and separating shear layers. The results agree qualitatively well with the published data on flow past a cylinder. We can see the small complex structures of the flow being captured by the GCCG scheme.

A numerical comparison between the GCCG scheme and the other methods was also carried out for this example. The results are quantified by computing the force coefficients

$$\text{Lift coefficient} = \frac{F_x}{\frac{1}{2}\rho_\infty u_\infty^2 D} = \int_0^{2\pi} \tau_2 \, \mathrm{d}\Gamma, \quad \text{drag coefficient} = \frac{F_y}{\frac{1}{2}\rho_\infty u_\infty^2 D} = \int_0^{2\pi} \tau_1 \, \mathrm{d}\Gamma$$

DOI: 10.1002/fld

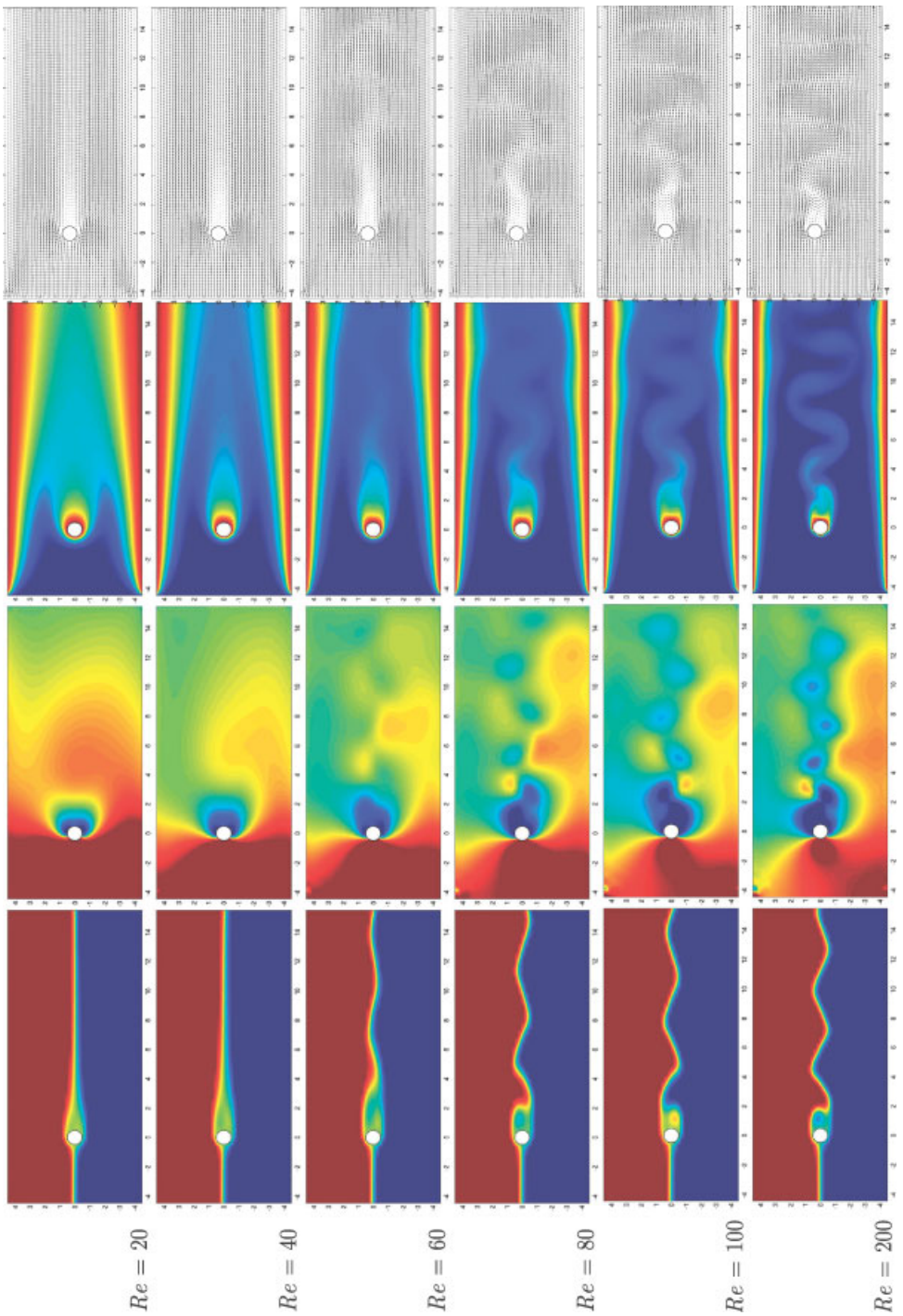

Figure 8. Stream function (first column), pressure distribution (second column), temperature field (third column) and velocity vectors (fourth column).

DOI: 10.1002/fld

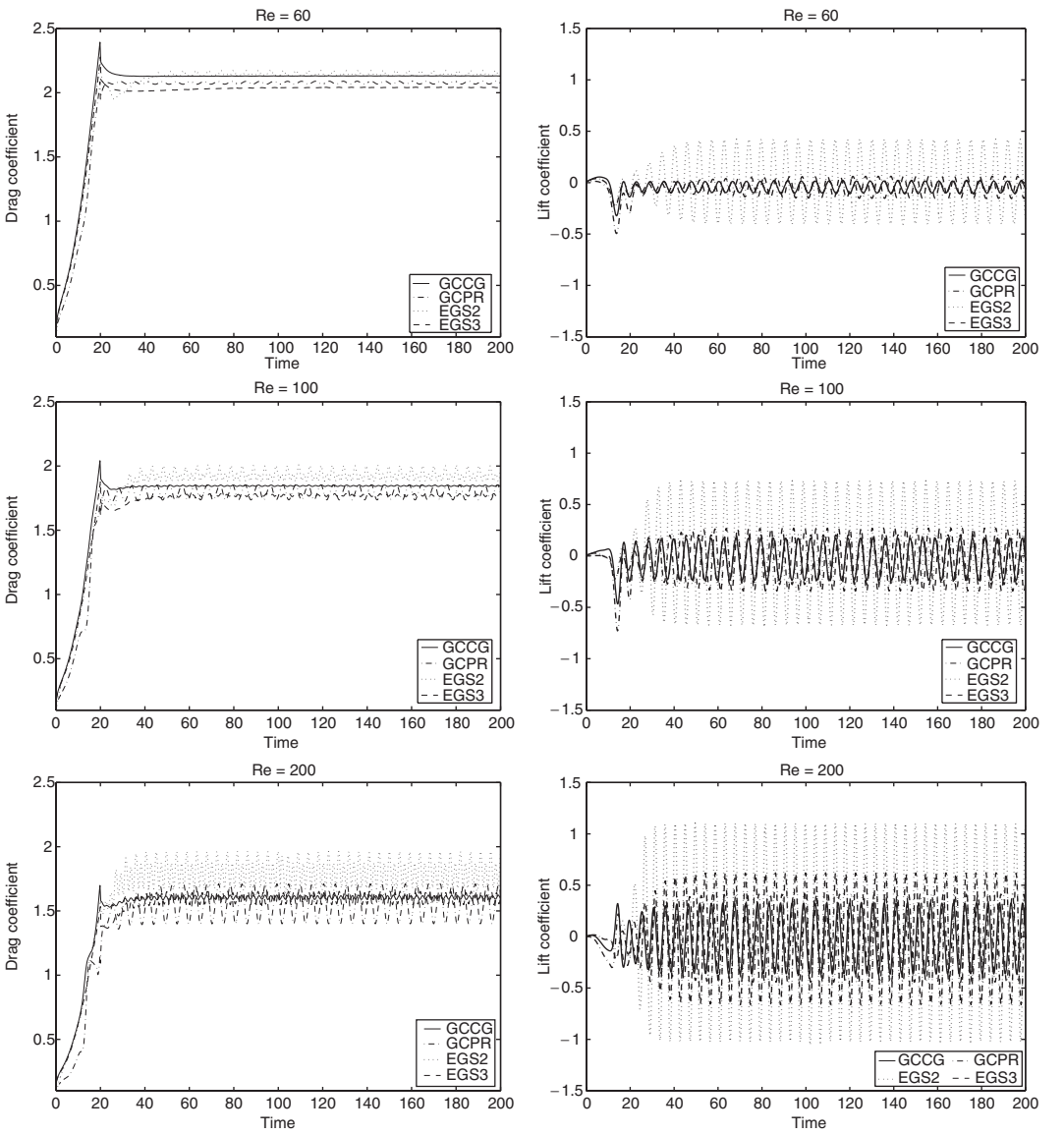

Figure 9. Drag and lift coefficients for the mixed convection at different Reynolds numbers.

where $\boldsymbol{\tau} = (\tau_1, \tau_2)^{\mathrm{T}}$ is the traction vector on the cylinder boundary Γ. The evolution in time of these force coefficients is shown in Figure 9 for the selected Reynolds numbers $Re = 60$, 100 and 200 at time $t = 200$. The results by EGPR scheme are not included in this figure because the scheme behaves badly for this mixed convection problem. As can be seen, at earlier time of simulation the lift coefficient is essentially zero, followed later by an oscillatory behaviour of rapidly increasing amplitude. Similarly, after an initial stabilization phase, the fluctuations in the drag coefficient

DOI: 10.1002/fld

Table VII. Comparison of computational times (in minutes) for the mixed convection problem.

Re	EGPR	GCPR	GCCG	EGS2	EGS3
20	7	6	9	19	22
40	9	7	10	21	27
60	12	10	17	36	39
80	15	13	25	41	51
100	19	15	32	49	63
200	27	21	44	65	85

Table VIII. Strouhal number for the mixed convection at $Re = 100$.

GCPR	GCCG	EGS2	EGS3
0.175	0.175	0.194	0.194

show a steady pattern along the considered time interval. The drag coefficient exhibits fluctuations of higher frequency than the lift coefficient. The periodic character of the coefficients in the figure should be noted. A dimensionless number, used in experimental studies, to quantify this periodic feature is the Strouhal number, $St = D/u_\infty \mathbb{T}$, where $\mathbb{T}$ is the time period. In Table VIII, we list the obtained Strouhal number for this test example at $Re = 100$ using the considered methods. In these results, $\mathbb{T}$ is the period of oscillation calculated from the time evolution of the drag and lift coefficients in Figure 9. We should mention that the corresponding experimental Strouhal number for the isothermal case is 0.16, see for example [25].

A simple inspection of Figure 9 shows that the EGS2 scheme exhibits the highest amplitudes in the drag and lift coefficients. The EGS3 result lies between the GCCG scheme and EGS2 scheme. The GCCG method appears to be superior to the Eulerian-based methods and does not exhibit the excessive dissipation reported in the Eulerian-based methods. The GCCG Strouhal number in Table VIII is identically equivalent to that of GCPR scheme, while it is inferior to the EGS2 and EGS3 schemes. Note that, the GCCG method produces reasonable Strouhal number when it is compared with the experimental one in [25] for isothermal case.

Table VII contains computational statistics for the mixed convection at the considered Reynolds numbers and at time $t = 200$. As in the case of natural convection, the overall computational work increases as the Reynolds number is increased. The clear indication from this table is that the CPU time used by the GCCG scheme approximately doubles when using the EGS3 scheme for the same *Re* number. The EGS3 method displays CPU times of roughly four times more than GCPR method.

From the simulated results of the considered schemes examined herein for the mixed convection flow past a cylinder, one may conclude the following: (i) the EGPR scheme fails to solve this test problem; (ii) the GCCG scheme is more accurate than GCPR scheme; (iii) the EGS2 scheme is comparable with the EGS3 scheme, and both provide convincing computed results in spite of some degree of numerical diffusion; (iv) the computational cost required for EGS2 and EGS3 schemes is much larger than the one required for GCPR and GCCG methods in a simulation with the same *Re* number.

DOI: 10.1002/fld

5. CONCLUSIONS

In this article we have presented a class of Galerkin-characteristic methods for solving natural and mixed convection problems. The methods combine the modified method of characteristics for time integration with Galerkin finite element for space discretization. The methods are formulated for the governing equations in primitive variables. We have considered both a projection-type and a direct-type procedures for the generalized Stokes/Boussinesq problem. A comparison with other Eulerian-based Galerkin finite element methods demonstrates the feasibility of the present Galerkin-characteristic algorithms to solve natural convection and mixed convection flows at high Rayleigh and Reynolds numbers, respectively.

The favourable performance of the present Galerkin-characteristic algorithms has been demonstrated using the example of natural convection in a squared cavity and the example of mixed convection flow past a circular cylinder. Numerical comparisons have been carried out for all the considered methods in terms of streamlines, velocity vectors, isotherms, vorticity contours and local Nusselt number plots. In both examples, the direct-type Galerkin-characteristic method shows high accuracy than the projection-type Galerkin-characteristic method. The results obtained show that the direct-type Galerkin-characteristics method is as accurate as conventional schemes based on Eulerian Galerkin splitting of the governing equations. The direct-type Galerkin-characteristic algorithm has the advantage of requiring less resources for the convection integration than an Eulerian-based Galerkin splitting method, typical of those widely used in Eulerian splitting algorithms for the incompressible Navier–Stokes equations. This fact, as well as its favourable stability properties, make it an attractive alternative for thermal Navier–Stokes solvers based on Galerkin-characteristic splitting.

Future work will concentrate on developing efficient solver for the associated linear systems and extension of these techniques to natural and mixed convection flows in three-space dimensions.

APPENDIX A

In this appendix we give a brief formulation of the Eulerian-based Galerkin methods used in the current work for comparison reasons.

A.1. Eulerian-based Galerkin projection (EGPR) scheme

Given the solution $\{\mathbf{u}^n, T^n, p^n\}$ at time t_n, the solution $\{\mathbf{u}^{n+1}, T^{n+1}, p^{n+1}\}$ is computed as follows:

1. Solve for $\bar{\mathbf{u}}^{n+1}$

$$\begin{aligned} \frac{\bar{\mathbf{u}}^{n+1}-\mathbf{u}^n}{\Delta t}+\mathscr{E}(\mathbf{u}^*,\bar{\mathbf{u}}^{n+\theta})+\gamma\nabla p^n-Pr\Delta\bar{\mathbf{u}}^{n+\theta}&=Pr\,Ra\,T^*\mathbf{e} \quad \text{in } \Omega\\ \bar{\mathbf{u}}^{n+1}&=\mathbf{0} \quad \text{on } \Gamma \end{aligned} \tag{A1}$$

2. Solve for $\bar{p}$ and $\mathbf{u}^{n+1}$

$$\begin{aligned} \frac{\mathbf{u}^{n+1}-\bar{\mathbf{u}}^{n+1}}{\Delta t}+\nabla\bar{p}&=\mathbf{0} \quad \text{in } \Omega\\ \nabla\cdot\mathbf{u}^{n+1}&=0 \quad \text{in } \Omega\\ \mathbf{n}\cdot\nabla\mathbf{u}^{n+1}&=0 \quad \text{on } \Gamma \end{aligned} \tag{A2}$$

DOI: 10.1002/fld

3. Solve for T^{n+1}

$$\begin{aligned} \frac{T^{n+1}-T^n}{\Delta t}+\mathbf{u}^{n+1}\cdot\nabla T^{n+\theta}-\Delta T^{n+\theta}&=0 \quad \text{in } \Omega \\ T^{n+1}&=T_{\mathrm{D}} \quad \text{on } \Gamma_{\mathrm{D}} \\ \mathbf{n}\cdot\nabla T^{n+1}&=0 \quad \text{on } \Gamma_{\mathrm{N}} \end{aligned} \tag{A3}$$

4. Update p^{n+1}

$$p^{n+1}=\gamma p^n+(1+\gamma)\bar{p}$$

The discretization for the convection term, $\mathscr{E}(\mathbf{u},\mathbf{v})$, is given by

$$\mathscr{E}(\mathbf{u},\mathbf{v})=(\mathbf{u}\cdot\nabla)\mathbf{v}+\tfrac{1}{2}(\nabla\cdot\mathbf{u})\mathbf{v} \tag{A4}$$

Here, $T^{n+\theta}$ and $\bar{\mathbf{u}}^{n+\theta}$ are defined as

$$T^{n+\theta}=\theta T^{n+1}+(1-\theta)T^n, \quad \bar{\mathbf{u}}^{n+\theta}=\theta\bar{\mathbf{u}}^{n+1}+(1-\theta)\mathbf{u}^n$$

whereas, T^* and $\mathbf{u}^*$ are given by

$$T^*=\tfrac{3}{2}T^n-\tfrac{1}{2}T^{n-1}, \quad \mathbf{u}^*=\tfrac{3}{2}\mathbf{u}^n-\tfrac{1}{2}\mathbf{u}^{n-1}$$

In our implementation, we used $\gamma=1$, $\theta=\frac{1}{2}$ and a pressure-Poisson problem of the form (20) is solved for $\bar{p}$. Details on standard projection methods can be found in [24, 27].

A.2. Eulerian-based Galerkin splitting (EGS2) scheme with two stages

Given the solution $\{\mathbf{u}^n, T^n, p^n\}$ at time t_n, the solution $\{\mathbf{u}^{n+1}, T^{n+1}, p^{n+1}\}$ is computed as follows:

1. Solve

$$\begin{aligned} \frac{\mathbf{u}^{n+\theta}-\mathbf{u}^n}{\theta\Delta t}+\mathscr{E}(\mathbf{u}^*,\mathbf{u}^n)+\nabla p^{n+\theta}-\alpha Pr\,\Delta\mathbf{u}^{n+\theta}&=\beta Pr\,\Delta\mathbf{u}^n+Pr\,Ra\,T^*\mathbf{e} \\ \nabla\cdot\mathbf{u}^{n+\theta}&=0 \quad \text{in } \Omega \\ \mathbf{u}^{n+\theta}&=\mathbf{0} \quad \text{on } \Gamma \end{aligned} \tag{A5}$$

2. Solve

$$\begin{aligned} \frac{\mathbf{u}^{n+1}-\mathbf{u}^{n+\theta}}{(1-\theta)\Delta t}+\mathscr{E}(\mathbf{u}^*,\mathbf{u}^{n+\theta})+\nabla p^{n+1}-\beta Pr\,\Delta\mathbf{u}^{n+1}&=\alpha Pr\,\Delta\mathbf{u}^{n+\theta}+Pr\,Ra\,T^*\mathbf{e} \\ \nabla\cdot\mathbf{u}^{n+1}&=0 \quad \text{in } \Omega \\ \mathbf{u}^{n+1}&=\mathbf{0} \quad \text{on } \Gamma \end{aligned} \tag{A6}$$

3. Solve (A3) to update T^{n+1}.

The order of accuracy in EGS2 scheme is determined by the selection of parameters θ, α and β. A simple selection leading to a second-order accurate scheme is $\theta=\alpha=\beta=\frac{1}{2}$, compare [17, 28] for more details.

DOI: 10.1002/fld

A.3. Eulerian-based Galerkin splitting (EGS3) scheme with three stages

Given the solution $\{\mathbf{u}^n, T^n, p^n\}$ at time t_n, the solution $\{\mathbf{u}^{n+1}, T^{n+1}, p^{n+1}\}$ is computed as follows:

1. Solve

$$\frac{\mathbf{u}^{n+\theta}-\mathbf{u}^n}{\theta\Delta t}+\mathscr{E}(\mathbf{u}^*,\mathbf{u}^n)+\nabla p^{n+\theta}-\alpha\,Pr\,\Delta\mathbf{u}^{n+\theta}=\beta\,Pr\,\Delta\mathbf{u}^n+Pr\,Ra\,T^*\mathbf{e}$$

$$\nabla\cdot\mathbf{u}^{n+\theta}=0 \quad \text{in } \Omega \tag{A7}$$

$$\mathbf{u}^{n+\theta}=\mathbf{0} \quad \text{on } \Gamma$$

2. Solve

$$\frac{\mathbf{u}^{n+1-\theta}-\mathbf{u}^{n+\theta}}{(1-2\theta)\Delta t}+\mathscr{E}(\mathbf{u}^*,\mathbf{u}^{n+1-\theta})+\nabla p^{n+\theta}-\beta\,Pr\,\Delta\mathbf{u}^{n+1-\theta}=\alpha\,Pr\,\Delta\mathbf{u}^{n+\theta}+Pr\,Ra\,T^*\mathbf{e} \tag{A8}$$

$$\mathbf{u}^{n+1-\theta}=\mathbf{0} \quad \text{on } \Gamma$$

3. Solve

$$\frac{\mathbf{u}^{n+1}-\mathbf{u}^{n+1-\theta}}{\theta\Delta t}+\mathscr{E}(\mathbf{u}^*,\mathbf{u}^{n+1-\theta})+\nabla p^{n+1}-\alpha\,Pr\,\Delta\mathbf{u}^{n+1}=\beta\,Pr\,\Delta\mathbf{u}^{n+1-\theta}+Pr\,Ra\,T^*\mathbf{e}$$

$$\nabla\cdot\mathbf{u}^{n+1}=0 \quad \text{in } \Omega \tag{A9}$$

$$\mathbf{u}^{n+1}=\mathbf{0} \quad \text{on } \Gamma$$

4. Solve (A3) to update T^{n+1}.

Here, the solution $\mathbf{u}^*$ is defined as

$$\mathbf{u}^*=\frac{2\theta-1}{\theta}\mathbf{u}^n+\frac{1-\theta}{\theta}\mathbf{u}^{n+\theta}$$

In our computations, we set $\theta=1-1/\sqrt{2}$, $\alpha=(1-2\theta)/(1-\theta)$ and $\beta=1-\alpha=\theta/(1-\theta)$. This selection yields a second-order accurate scheme and has been studied in [17, 24, 29] among others. Note that, the integration of Equations (A1)–(A9) for triangular elements is easy and described in many text books, compare [18] among others.

ACKNOWLEDGEMENTS

M. El-Amrani acknowledges the support from Universidad Rey Juan Carlos (Grant no. GDV-04-3) for his visit to Technomathematics Group in Kaiserslautern University during which, part of this work was performed. The partial support for M. Seaïd by the German Research Foundation (DFG) is also acknowledged.

DOI: 10.1002/fld

REFERENCES

1. Temperton C, Staniforth A. An efficient two-time-level semi-Lagrangian semi-implicit integration scheme. *Quarterly Journal of Royal Meteorological Society* 1987; **113**:1025–1039.
2. Pironneau O. On the transport-diffusion algorithm and its applications to the Navier–Stokes equations. *Numerische Mathematik* 1982; **38**:309–332.
3. Douglas TF, Russell J. Numerical methods for convection dominated diffusion problems based on combining the method of characteristics with finite elements or finite differences. *SIAM Journal on Numerical Analysis* 1982; **19**:871–885.
4. Bermejo M, El-Amrani R. A finite element semi-Lagrangian explicit Runge–Kutta–Chebyshev method for convection dominated reaction–diffusion problems. *Journal of Computational and Applied Mathematics* 2003; **154**:27–61.
5. El-Amrani M, Seaïd M. Convergence and stability of finite element modified method of characteristics for the incompressible Navier–Stokes equations, submitted for publication.
6. Süli E. Convergence and stability of the Lagrange–Galerkin method for the Navier–Stokes equations. *Numerische Mathematik* 1988; **53**:459–483.
7. Süli A, Ware E. A spectral method of characteristics for hyperbolic problems. *SIAM Journal on Numerical Analysis* 1991; **28**:423–445.
8. El-Amrani M, Seaïd M. Weakly compressible and advection approximations of incompressible viscous flows. *Communications in Numerical Methods in Engineering* 2006; **22**:831–847.
9. Seaïd M. On the quasi-monotone modified method of characteristics for transport-diffusion problems with reactive sources. *Journal of Computational Methods and Applied Mathematics* 2002; **2**:186–210.
10. Seaïd M. Semi-Lagrangian integration schemes for viscous incompressible flows. *Journal of Computational Methods and Applied Mathematics* 2002; **4**:392–409.
11. Roberts PH. Convection in horizontal layers with internal heat generation: theory. *Journal of Fluid Mechanics* 1967; **30**:33–49.
12. Jaluria Y. *Natural Convection Heat and Mass Transfer*. Pergamon Press: Oxford, 1980.
13. Bercovier O, Pironneau M. Error estimates for finite element solution of the Stokes problem in the primitive variables. *Numerische Mathematik* 1979; **33**:211–224.
14. Verfürth R. Error estimates for a mixed finite element approximation of the Stokes equation. *RAIRO-Analyse Numerique* 1984; **18**:175–182.
15. Allievi A, Bermejo R. A generalized particle search-locate algorithm for arbitrary grids. *Journal of Computational Physics* 1997; **132**:157–166.
16. Seaïd M, El-Amrani M. Lagrange–Galerkin method for unsteady free surface water waves. *Computing and Visualization in Science* 2006, in press.
17. Dean R, Glowinski EJ. On some finite elements methods for the numerical simulation of incompressible viscous flow. In *Incompressible Computational Fluid Dynamics*, Gunzburger MD, Nicolaides RA (eds). Cambridge University Press: Cambridge, 1993.
18. Johnson C. *Numerical Solution of Partial Differential Equations by the Finite Element Method*. Cambridge University Press: Cambridge, London, 1987.
19. De Valhl Davis D. Natural convection of air in a square cavity: a benchmark solution. *International Journal for Numerical Methods in Fluids* 1983; **3**:249–264.
20. Manzari MT. An explicit finite element algorithm for convective heat transfer problems. *International Journal for Numerical Methods in Heat and Fluid Flow* 1999; **9**:860–877.
21. Mayne DA, Usmani AS, Carpper M. *h*-adaptive finite element solution of high Rayleigh number thermally driven cavity problem. *International Journal for Numerical Methods in Heat and Fluid Flow* 2000; **10**:598–615.
22. Wan DC, Patnaik SV, Wei GW. A new benchmark quality solution for the buoyancy-driven cavity by discrete singular convolution. *Numerical Heat Transfer*, *Part B* 2001; **40**:199–228.
23. Schäfer S, Turek M. Benchmark computations of laminar flow around a cylinder. *Notes on Numerical Fluid Mechanics* 1996; **52**:547–566.
24. Simo J, Armero F. Unconditional stability and long-term behavior of transient algorithms for the incompressible Navier–Stokes and Euler equations. *Computer Methods in Applied Mechanics and Engineering* 1994; **111**: 111–154.
25. Graham MR. The effects of waves on vortex shedding from cylinders. *IUTAM Symposium on Buff-Body Wakes*, *Dynamics and Instabilities*, Gottingen, Germany, 1992.

DOI: 10.1002/fld

26. Kieft RN, Rindt CM, van Steenhoven AA, Van Heijst JF. On the wake structure behind a heated horizontal cylinder in cross-flow. *Journal of Fluid Mechanics* 2003; **486**:189–211.
27. Chorin AJ. Numerical solution of the Navier–Stokes equations. *Mathematics of Computation* 1968; **22**:22.
28. Smith D, Silvester A. Implicit algorithms and their linearization for the transient incompressible Navier–Stokes equations. *SIAM Journal on Numerical Analysis* 1997; **17**:527–545.
29. Klouček F, Rys P. Stability of the fractional step θ-scheme for the nonstationary Navier–Stokes equations. *SIAM Journal on Numerical Analysis* 1994; **31**:1312–1335.

DOI: 10.1002/fld